A&A 524, A38 (2010)
DOI: 10.1051/0004-6361/201015394

Astronomy & Astrophysics

Parallaxes and physical properties of 11 mid-to-late T dwarfs

F. Marocco[1,2], R. L. Smart[1], H. R. A. Jones[3], B. Burningham[3], M. G. Lattanzi[1], S. K. Leggett[4], P. W. Lucas[3], C. G. Tinney[5], A. Adamson[6], D. W. Evans[7], N. Lodieu[8,9], D. N. Murray[3], D. J. Pinfield[3], and M. Tamura[10]

[1] INAF/Osservatorio Astronomico di Torino, Strada Osservatorio 20, 10025 Pino Torinese, Italy
e-mail: fmarocco@libero.it, smart@oato.inaf.it
[2] Università degli Studi di Torino, Facoltà di Scienze MFN – Dipartimento di Fisica, via Pietro Giuria 1, 10126 Torino, Italy
[3] Centre for Astrophysics Research, Science and Technology Research Institute, University of Hertfordshire, Hatfield AL10 9AB, UK
[4] Gemini Observatory, Northern Operations Center, 670 N. Aohoku Place, Hilo, HI 96720, USA
[5] Anglo-Australian Observatory, PO Box 296, Epping, NSW1710, Australia
[6] Joint Astronomy Centre, 660 North Aohoku Place, Hilo, HI 96720, USA
[7] Institute of Astronomy, Madingley Road, Cambridge CB3 0HA, UK
[8] Instituto de Astrofísica de Canarias, vía Láctea s/n, 38205 La Laguna, Tenerife, Spain
[9] Departamento de Astrofísica, Universidad de La Laguna (ULL), 38205 La Laguna, Tenerife, Spain
[10] National Astronomical Observatory of Japan, 2-21-1 Osawa, Mitaka, Tokyo 181-8588, Japan

Received 14 July 2010 / Accepted 20 August 2010

ABSTRACT

Aims. We present parallaxes of 11 mid-to-late T dwarfs observed in the UKIRT Infrared Deep Sky Survey. We use these results to test the reliability of model predictions in magnitude–color space, determine a magnitude-spectral type calibration, and, estimate a bolometric luminosity and effective temperature range for the targets.
Methods. We used observations from the UKIRT WFCAM instrument pipeline processed at the Cambridge Astronomical Survey Unit. The parallaxes and proper motions of the sample were calculated using standard procedures. The bolometric luminosity was estimated using near- and mid-infrared observations with two different methods. The corresponding effective temperature ranges were found adopting a large age-radius range.
Results. We show the models are unable to predict the colors of the latest T dwarfs indicating the incompleteness of model opacities for NH_3, CH_4 and H_2 as the temperature declines. We report the effective temperature ranges obtained.

Key words. stars: low-mass – brown dwarfs – stars: fundamental parameters – stars: distances – astrometry

1. Introduction

Since the first discovery of a T dwarf by Nakajima et al. (1995) understanding the atmospheric processes and the role of chemical composition for such low temperature objects has been very challenging. This remains an important goal, particularly given that we consider these objects to be the link between stars and giant exoplanets, therefore, their properties offer insights into formation and evolution of planetary systems.

One of the fundamental parameters required to determine the physical properties and to constrain theoretical models of celestial objects is distance. Until now, only a few late T dwarfs have known distances: Wolf940B (Harrington & Dahn 1980), HD3651B (Perryman et al. 1997), 2MASS J0415-0935 (Vrba et al. 2004), 2MASS J0939-2448 (Burgasser et al. 2008), ULAS J003402.77-005206.7 (Smart et al. 2010). Thus the theoretical models have been constrained by the earlier T dwarfs. The UKIRT Infrared Deep Sky Survey (Lawrence et al. 2007, hereafter UKIDSS) is revealing large numbers of new T dwarfs (Burningham et al. 2010; Lodieu et al. 2009a,b; Burningham et al. 2008; Pinfield et al. 2008; Chiu et al. 2008; Lodieu et al. 2007; Kendall et al. 2007) and in particular cool T8/T9 dwarfs. An important follow up for the coolest T dwarfs observed in the UKIDSS is the determination of their parallax. As shown in Smart et al. (2010, hereafter SJL10) for ULAS J003402.77-005206.7 using the UKIDSS discovery image it is possible to reduce the time required to determine a preliminary parallax and here we present 10 additional objects.

In this contribution all targets will be referred to by the discovery acronym and right ascension short format hence ULAS J003402.77-005206.7 becomes ULAS 0034, the full-names are given in Table 1. In Sect. 2 we describe the observations and procedures and in Sect. 3 we report the results for the 11 targets. In Sect. 4 we compare these results to current models and in Sect. 5 we calculate $L_{\rm bol}$ and $T_{\rm eff}$ of the objects in the sample. Finally in Sect. 6 we discuss the results obtained.

2. Observations and reduction procedures

The observations for the parallax determination began in 2007 and the target list of 11 objects was drawn from confirmed T dwarfs observed at that time in the UKIDSS Large Area Survey. In Table 1 we list the objects along with MKO magnitudes (Tokunaga et al. 2002) and near-infrared (hereafter NIR) spectral types. The NIR spectral type classification follows the scheme described in Burgasser et al. (2006a). The only object with an already published parallax was SDSS 0207 which was included because the USNO parallax had a large relative error (~28%, Vrba et al. 2004).

The procedures for observing, image treatment and parallax determination follow those described in SJL10. In that paper the

Table 1. Infrared magnitudes and spectral types of the 11 targets.

Full name	z_{AB}	Y	J	H	K	Sp. Type	Refs. (D,P,T)
ULAS J003402.77-005206.7	22.11 ± 0.05	18.90 ± 0.10	18.15 ± 0.03	18.49 ± 0.04	18.48 ± 0.05	T9	1,1,6
CFBDS J005910.90-011401.3	21.93 ± 0.05	18.82 ± 0.02	18.06 ± 0.03	18.27 ± 0.05	18.63 ± 0.05	T9	2,2,6
SDSS J020742.48+000056.2	20.11 ± 0.60	17.94 ± 0.03	16.75 ± 0.01	16.79 ± 0.04	16.71 ± 0.05	T4.5	3,(4,7),8
ULAS J082707.67-020408.2	...	18.29 ± 0.05	17.19 ± 0.02	17.44 ± 0.05	17.52 ± 0.11	T5.5	4,4,4
ULAS J090116.23-030635.0	...	18.82 ± 0.05	17.90 ± 0.04	18.46 ± 0.13	> 18.21	T7.5	4,4,4
ULAS J094806.06+064805.0	...	20.03 ± 0.14	18.85 ± 0.07	19.46 ± 0.22	> 18.62	T7	4,4,4
ULAS J101821.78+072547.1	...	18.90 ± 0.08	17.71 ± 0.04	17.87 ± 0.07	18.12 ± 0.17	T5	4,4,4
ULAS J115038.79+094942.8	22.44 ± 0.10	19.92 ± 0.08	18.68 ± 0.04	19.23 ± 0.06	19.06 ± 0.05	T6.5p	5,5,5
ULAS J131508.42+082627.4	22.82 ± 0.10	20.00 ± 0.08	18.86 ± 0.04	19.50 ± 0.10	19.60 ± 0.12	T7.5	5,5,5
ULAS J133553.45+113005.2	22.04 ± 0.10	18.81 ± 0.04	17.90 ± 0.01	18.25 ± 0.01	18.28 ± 0.03	T9	6,6,6
ULAS J223955.76+003252.6	...	19.94 ± 0.17	18.85 ± 0.05	19.10 ± 0.10	18.88 ± 0.06	T5.5	4,4,4

Notes. $YJHK$ are in the MKO Vega photometric system, while z is in AB system. The uncertainty in the spectral type is ± 0.5.

References. (D = Discovery, P = Photometry, T = Spectral Type): 1– Warren et al. (2007); 2– Delorme et al. (2008); 3– Geballe et al. (2002); 4– Lodieu et al. (2007); 5– Pinfield et al. (2008); 6– Burningham et al. (2008); 7– Knapp et al. (2004); 8– Burgasser et al. (2006a).

parallax observations of ULAS 0034 maintained the same target position as the discovery image and were aligned using a simple linear transformation. Assuming the astrometric distortion pattern does not change, the use of the discovery image as part of the parallax solution allows a much shorter dedicated observational campaign to obtain a precise parallax. For CFBDS 0059, SDSS 0207, ULAS 0948 and ULAS 2239 this was not possible because the target was very close to a chip edge in the first UKIDSS image. The WFCAM astrometric distortion is significant, so moving the reference frame on the focal plane results in poorer astrometric transformations (i.e. larger residuals in the solutions) and so in this situation those frames that are significantly offset are given lower weight.

Initially all observations were made with the same total exposure time of 400 s. For this exposure, in the case of the anonymous stars in the field of ULAS 0034, the centroiding precision is a constant 20 mas until around $J = 18.4$ and deteriorates quickly to 60 mas at $J = 19.2$ (Fig. 2 in SJL10). To ensure that centroiding precision is optimal even in poor observing conditions we have increased the exposure times to 710 s for the faint targets (ULAS 0034, 0948, 1150, 1315, 2239 and CFBDS 0059). The precision of the final solutions for the faint targets reflects the poor quality of some of the earlier 400 s observations.

In Fig. 1 we plot the solution of ULAS 0901 (top panel) and 1315 (bottom panel) which are objects of similar distances and observational history but with magnitudes of 17.90 and 18.86 respectively, e.g. straddling the precision borderline, to show high and low quality solutions.

3. Results

The astrometric parameters derived for the 11 targets are in Table 2. For each one we report: target name, position (J2000), number of reference stars, number of observations used, absolute parallax, proper motion components, tangential velocity, the time span covered by the observations and the relative-to-absolute parallax correction applied.The proper motion of the targets have all been brought to an absolute system using the galaxies in the field.

The relative errors for most of the targets are less than 10%. Observations are continuing and we hope to be able to reduce them to 5% by the end of the campaign. Significant exceptions are ULAS 1150, 1315 and 2239 which are also amongst the faintest objects under study, hence degraded the most by the borderline signal-to-noise in the early observations. In addition, parallax observations of ULAS 2239 were shifted from the discovery image position lowering the weight of the first point.

In Table 3 we compare the astrometric distances obtained here with the estimated ones given in the discovery paper of each object. The estimations were made with different techniques and the reader is referred to the discovery papers (see footnote to Table 1) for further details. The discovery distance range is usually much larger than our measured one and is overestimated for the late-Ts. This comparison underlines the need for measured parallaxes that are model independent.

4. Model fitting

In Figs. 2 and 3 we present four color - absolute magnitude diagrams for a sample of L and T dwarfs with $M_J > 12$ and $M_K > 12$ respectively. The 11 targets are plotted as filled circles. Parallaxes and magnitudes of the other objects are from two online archives:

1) The L/T dwarf archive maintained by S. K. Leggett (`http://staff.gemini.edu/~sleggett/2010_phot_tab.txt`, hereafter Leggett archive): This archive contains a compendium of 225 objects with MKO $YJHKL'M'$ magnitudes and IRAC [3.55], [4.49], [5.73] and [7.87] magnitudes. Where used these objects are plotted as filled squares.
2) The M/L/T dwarf archive (`www.dwarfarchives.org`, hereafter Dwarf archive): This is an on line compendium of all published L/T dwarfs and selected M dwarfs. As of 10/01/2010 there were 752 L & T dwarfs, reporting JHK magnitudes, parallaxes and proper motions. Where used these objects are plotted as filled triangles.

To make Figs. 2 and 3 clearer we omitted the error bars on the literature objects. An indication of the typical uncertainty on these points is given by the black cross above the legend.

All magnitudes are in the MKO system and preferentially taken from the Leggett archive as they are measured directly in that system. The majority of the infrared magnitudes in the Dwarf archive are in the 2MASS system and when needed we use the relations in Stephens & Leggett (2004) to convert to the MKO system.

Colored lines in Figs. 2 and 3 are the model predictions by Burrows et al. (2006, hereafter BSH06) and Allard et al. (2003, 2007, 2009, hereafter BTSettl09). BSH06 tracks covers the temperature range 700–2000 K, with $\log[g] = 4.5$, 5.0, 5.5 and

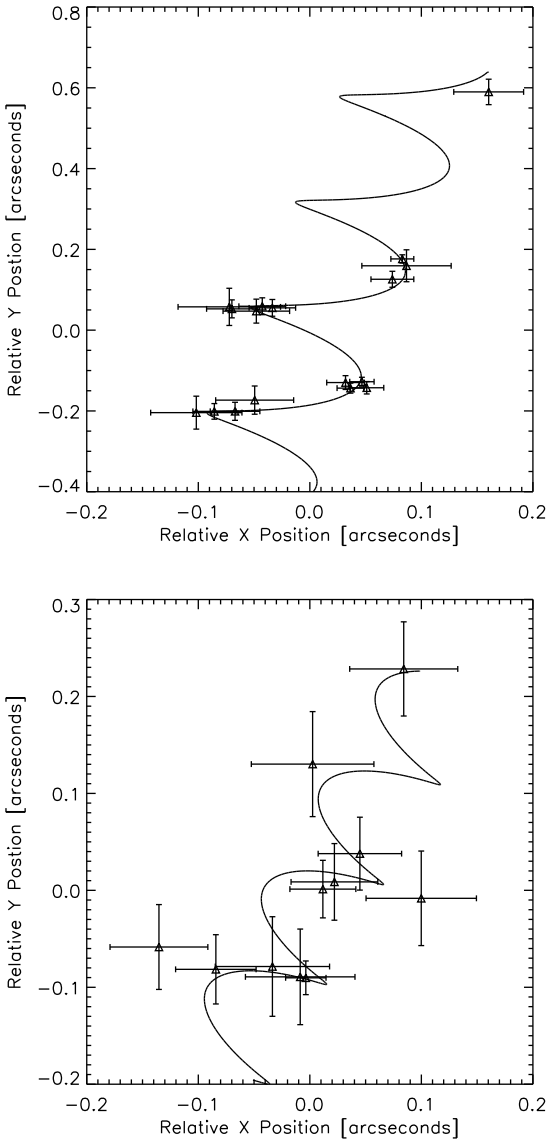

Fig. 1. Observations for the targets ULAS 0901 (*top panel*) and 1315 (*bottom panel*). The highest point is the discovery image. The observational history and distance of these two targets are similar but they differ by a magnitude in apparent brightness. The solution shows the effect of low signal-to-noise observations in the beginning of the parallax sequence.

[Fe/H] = – 0.5, 0, +0.5. BTSettl09 covers the range 500–780 K, with log[g] = 4.5, 5.0, 5.25 and [Fe/H] = – 0.2, 0, +0.2. For a given metallicity (indicated in the plots by a given color) log[g] increases from left to right in $J-H$, while it increases from right to left in $J-K$.

Model colors and magnitudes were obtained by convolving the theoretical spectra with the UKIDSS filter profiles (Hewett et al. 2006) to calculate fluxes. We interpolate the model spectra with a spline to have the same binning as the filter profiles, apply the selected profile, and integrate to obtain the total flux. The integrated fluxes were then converted into an absolute magnitude using as a zero point a Vega spectrum treated the same way.

The absolute magnitudes plotted in Figs. 2 and 3 require from the models the flux at 10 pc. The BSH06 models supply the flux at the surface of the object and at 10 pc, the latter calculated assuming the radius-log(g) – $T_{\rm eff}$ relation from Burrows et al. (1997). The BTSettl09 models provide only the flux at the surface of the object, to find the flux at 10pc we assume the radii from Baraffe et al. (2003) corresponding to the model log(g) and effective temperature.

In Figs. 2 and 3 we note that the BTSettl09 tracks for high and low metallicity are swapped in the different color spaces. In J-H space tracks for high metallicity are bluer than the low metallicity ones, while in $J-K$ they are redder. This follows the trend suggested by BSH06 tracks for higher temperature, and can be seen also in the models of Saumon & Marley (2008). Due to this swap, the predictions for the T9 dwarfs are incompatible in the two color spaces, i.e. they predict high gravity – low metallicity in $J-H$ and low gravity – high metallicity in $J-K$. Moreover, the T9s are redder than predicted by the theoretical models, especially in $J-K$. This failure may be due to an incorrect prediction of the flux emitted in the H and K-band resulting from known opacity deficiencies in modeling the collision-induced absorption of H_2 and the wing of the K I doublet resonance, and the lack of an appropriate list of absorption lines of CH_4 and NH_3 at such low temperatures (Leggett et al. 2010).

The predictions for earlier objects are consistent in the two color spaces, but in Fig. 2 they tend to slightly underestimate the magnitudes of the T6.5-T7s. Further discussion on the models predictions and individual objects is in Sect. 6.

In Fig. 4 we present three absolute magnitude – IR spectral type diagrams. The IR spectral type classification follows the scheme described in Geballe et al. (2002) for L dwarfs and the scheme described in Burgasser et al. (2006a) for T dwarfs. The over plotted curves are polynomial fits derived in Liu et al. (2006), with the dotted line representing the polynomial obtained excluding from the fit all the known and possible binaries, while the dashed line is the one obtained excluding only the known binaries. Possible binaries were selected by Liu et al. based on their relatively high $T_{\rm eff}$ compared to objects of similar spectral type in the Golimowski et al. (2004) measurements. One of the possible binaries indicated by Liu et al. (SDSS J1021-0304) was confirmed as a binary by Burgasser et al. (2006b), so now is plotted as a known binary. Following the convention used before, filled circles are the 11 targets and squares are objects from the Leggett archive, while blue objects are known binaries and green objects are possible binaries. The trend for T 8.5 and T9 is an extrapolation of the Liu et al polynomial, since their sample consisted of objects between L0 and T8.

The 11 targets indicate a steeper trend in the sequence beyond T8 than the extrapolation of the Liu et al. polynomial. In Fig. 4 the red lines are our 4-th order polynomials fit to the data including the new objects presented here, but excluding the 14 objects without magnitude naturally in the MKO system. This choice was made as the Stephens & Leggett (2004) transformations from the 2MASS to the MKO system were derived using hotter objects and employing them may introduce systematic errors in the resulting fit of the cooler objects. In Table 4 we list the coefficients and errors of the fit. The difference between the two fits with and without possible binaries is reduced compared to Liu et al., probably because of the smaller statistical weight of the possible binaries in this study (5 over a total sample of 61 objects) with respect to Liu et al. (6 over 43). As the sample of late T dwarfs is still small, identification of possible binaries in this region may be incomplete.

We also tested polynomials from 3rd to 10th order but after 4th order there was no significant improvement in the sigma of the fit.

Table 2. Parallaxes and proper motions of the 11 targets.

Target	α (h:m:s)	δ (d:m:s)	N*, obs	$\pi^{abs} \pm \sigma_\pi$ (mas)	$\mu_\alpha^{abs} \pm \sigma_{\mu_\alpha}$ (mas/y)	$\mu_\delta^{abs} \pm \sigma_{\mu_\delta}$ (mas/y)	V_{tan} (km s^{-1})	Time span (years)	COR (mas)
ULAS 0034	0:34:02.7	–0:52:07.8	135, 17	78.0 ± 3.6	–18.5 ± 3.2	–363.3 ± 3.6	21.7 ± 1.0	3.81	1.24
CFBDS 0059	0:59:10.9	–1:14:01.4	70, 13	108.2 ± 5.0	878.8 ± 8.4	50.5 ± 4.8	38.6 ± 1.8	2.69	1.19
SDSS 0207	2:07:42.9	+0:00:56.0	47, 17	29.3 ± 4.0	158.8 ± 3.0	–14.3 ± 3.9	25.8 ± 3.6	3.70	1.37
ULAS 0827	8:27:07.6	–2:04:08.4	418, 17	26.0 ± 3.1	26.8 ± 2.7	-108.9 ± 2.3	20.5 ± 2.5	3.94	0.87
ULAS 0901	9:01:16.2	–3:06:35.4	241, 19	62.6 ± 2.6	–38.6 ± 2.3	-261.2 ± 2.8	20.0 ± 0.8	3.90	1.00
ULAS 0948	9:48:06.1	+6:48:04.5	152, 15	27.2 ± 4.2	199.4 ± 7.0	–273.9 ± 6.2	59.1 ± 9.3	1.58	0.98
ULAS 1018	10:18:21.7	+7:25:46.8	198, 14	25.0 ± 2.0	–183.7 ± 2.6	–15.1 ± 3.1	34.9 ± 2.8	2.00	1.04
ULAS 1150	11:50:38.7	+9:49:42.8	105, 10	16.8 ± 7.5	–107.6 ± 17.1	–31.9 ± 4.5	31.7 ± 14.9	2.91	1.09
ULAS 1315	13:15:08.4	+ 8:26:27.0	213, 11	42.8 ± 7.7	–60.2 ± 8.3	–95.8 ± 10.0	12.5 ± 2.5	3.07	0.95
ULAS 1335	13:35:53.4	+11:30:05.1	196, 8	96.7 ± 3.2	–196.9 ± 4.9	–201.0 ± 6.3	13.8 ± 0.5	2.18	0.95
ULAS 2239	22:39:55.7	+0:32:52.7	120, 15	10.4 ± 5.2	125.3 ± 5.4	–108.4 ± 5.2	75.7 ± 37.8	2.95	0.96

Notes. In the fourth column we report the number of reference stars (N*) and the number of observations (obs). In the ninth column we report the time span covered by the observations and in the last one the relative-to-absolute parallax correction (COR).

Table 3. The 1-sigma distance range obtained here compared to those estimated in the discovery papers.

Name	Astrometric distance (pc)	Discovery distance (pc)	Discovery reference
ULAS 0034	12.2–13.4	14–24	1
CFBDS 0059	8.8–9.6	8–18	2
ULAS 0827	33.8–43.0	24–39	3
ULAS 0901	15.3–16.7	21–33	3
ULAS 0948	31.1–42.5	38–60	3
ULAS 1018	36.8–43.2	33–52	3
ULAS 1150	32.9–86.1	42–60	4
ULAS 1315	19.2–27.6	34–48	4
ULAS 1335	10.0–10.6	8–12	5
ULAS 2239	48.0–144.2	52–83	3

References. 1– Warren et al. (2007); 2– Delorme et al. (2008); 3– Lodieu et al. (2007); 4– Pinfield et al. (2008); 5– Burningham et al. (2008).

5. Luminosity and effective temperature

Next we calculate an effective temperature range for our targets. To do this we used the classical Stefan-Boltzmann law:

$$L_{bol} = 4\pi\sigma R^2 T_{eff}^4 \quad (1)$$

hence to calculate the temperature we need to know the radius and the bolometric luminosity of each object.

To determine a radius, we consider the models of Baraffe et al. (2003) we see that the radius of T dwarfs decreases rapidly when the object is very young but after 0.5 Gyr it is very constant. Therefore if we can constrain the age of our objects we can use these models to constrain the radius. In Fig. 5 we report the galactic velocity components (U, V, W) of the 11 targets. The components were calculated from the proper motions in Table 2 assuming a radial velocity range of +80/–80 km s^{-1}. Given this large range in V_{rad}, the uncertainty in the proper motion becomes negligible, so we ignore it in this calculation. The overplotted box is the locus of very young objects (age < 0.1 Gyr, Zuckerman & Song 2004) while the ellipsoid is the locus of young disk objects (age < 0.5 Gyr, Eggen 1969). Even given this very conservative range in possible radial velocities no objects fall in the boxed area or in the ellipsoid area in all three components. We therefore conclude that all objects are older than 0.5 Gyr. For the 0.5–10 Gyr models from Baraffe et al. (2003) we find the radius has a range of 1.2–0.8 R_{Jup} (in a temperature range of 500–2000 K). This is also consistent with the radii predicted by Burrows et al. (1997) models for objects of the same age and temperature.

To calculate the bolometric flux (and hence the luminosity) we combined the available measured spectrum of each object (Burningham et al. 2008; Leggett et al. 2009) flux calibrated using UKIDSS *YJHK* photometry, with the model spectra. For ULAS 0034 and 1335 we have the spectrum in the near- and mid-infrared (hereafter MIR) region, while for the other objects we only have the NIR portion. To find the bolometric flux we use model spectra to estimate the flux where we do not have observations: at short wavelengths ($\lambda < 1.0\ \mu$m), and, for ULAS 0034 and 1335, in the region between the near- and mid-infrared spectrum (2.4 μm < λ < 7.5 μm) or, for the other targets, in the entire portion from 2.4 μm to 15 μm. The flux emitted beyond 15 μm was estimated assuming a Rayleigh-Jeans tail.

The models used are the already mentioned BTSettl09 and the non-equilibrium models by Hubeny & Burrows (2007), covering the temperature range from 700 to 1900 K, for log[g] = 4.5,5.0 and 5.5, assuming values of $K_{zz} = 10^2$, 10^4 and 10^6 cm^2 s^{-1} (eddy diffusion coefficient), for different speed of the CO/CH$_4$ reaction (for further details see Hubeny & Burrows 2007; Saumon et al. 2006 and reference therein).

For each object we took the models in a wide range of temperature (±200 K around the temperature predicted by the temperature-type relation given by Stephens et al. 2009[1]), gravity (log[g] from 4.5 to 5.5) and metallicity ([Fe/H] from –0.2 to +0.2) and we scaled them using the available magnitudes (listed in Tables 1 and 5). For each model we took the average scaling factor obtained and we compared it with the range given by the known distance and the radius range adopted (i.e. the square of 0.8 R_{Jup}/distance ±3σ – the square of 1.2 R_{Jup}/distance ±3σ). We discarded the models whose average scaling factor was out of this pseudo-3σ range. We joined each one of the remaining spectra with the measured one and we calculate the resulting bolometric flux, the luminosity and hence the temperature range (corresponding to the radius range). Then we compared the temperature obtained with the one associated with the model employed. We discarded those models whose temperature differed by more than 100 K from the temperature range obtained. Finally we assumed the mean flux given by the remaining models as our final estimation and hence we calculate the luminosity and the temperature range.

[1] Except for the T9s, since we don't have theoretical spectra for temperatures lower than 500 K.

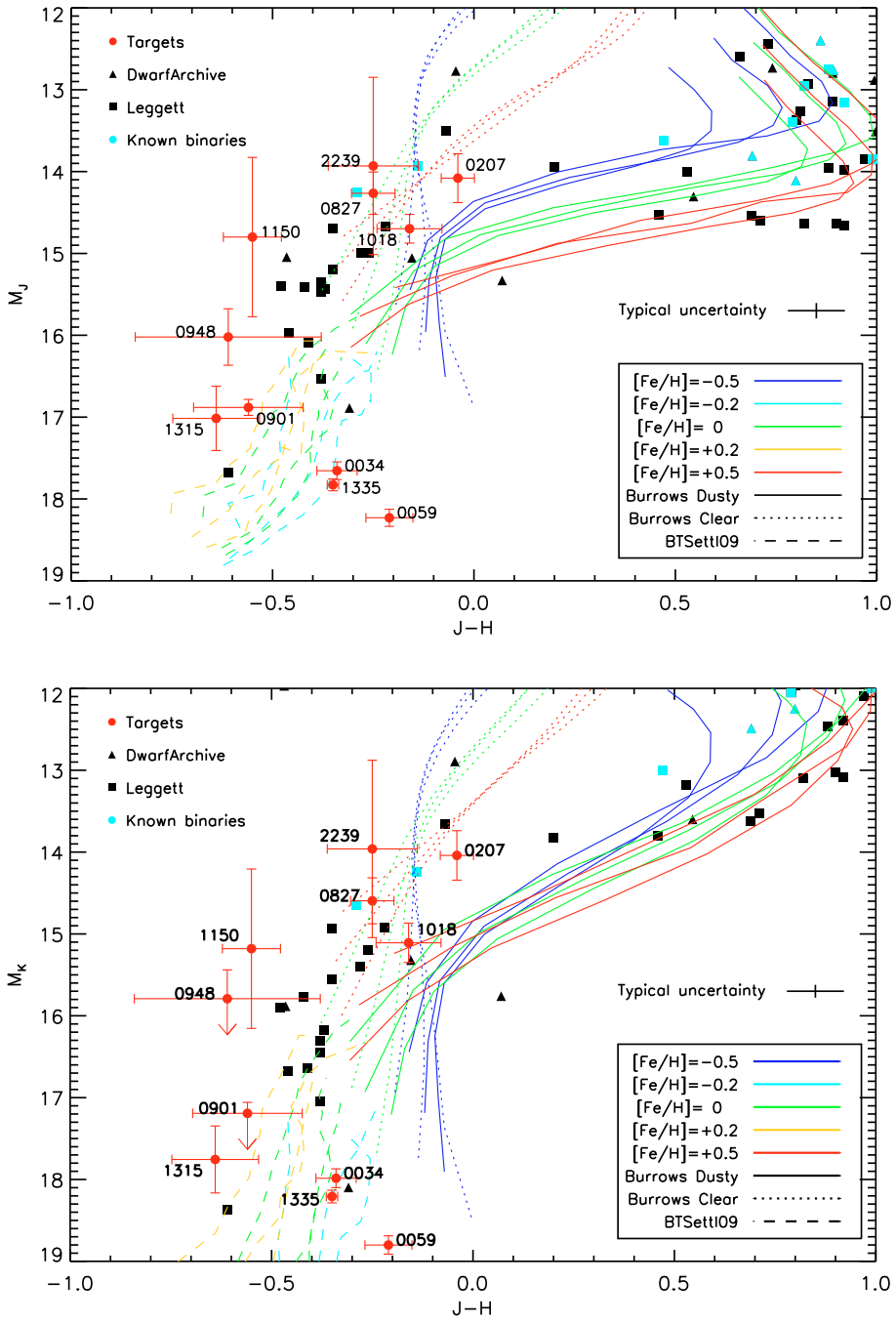

Fig. 2. Color–magnitude diagrams for a sample of L and T dwarfs. The colored lines are theoretical tracks from BSH06 and BTSettl09, for different gravities and metallicities. For each metallicity, the gravity increases *from left to right*, assuming the values 4.5,5.0,5.5 for BSH06 tracks and 4.5, 5.0, 5.25 for BTSettl09. The 11 targets presented here are plotted as filled circles with their associated error bars, the Dwarf archive objects are plotted as triangles and the Leggett archive objects as squares. All magnitudes in the MKO system. The cross above the legend indicates the typical uncertainty on the literature objects.

The uncertainty in the flux is given by the spread in values plus a 3% uncertainty in the magnitudes used to calibrate the observed spectra and to scale the model ones. The uncertainty in the luminosity and the temperature is the result of the standard propagation of the errors on the flux and the distance, ignoring the uncertainty in the radius, given the wide range adopted.

The results are shown in Table 6. In the first column we indicate the target short name, in the second one its spectral type, in the third the temperature estimated using the temperature-spectral type relation given by Stephens et al. (2009), in the fourth the range of models employed, in the fifth the range of models kept after the first step (so after comparing the scaling factors), in the sixth the range of models kept after the second step (so after comparing the temperatures), in the seventh our assumed bolometric flux, in the eighth the associated luminosity and in the last the temperature range obtained.

We note that the use of MIR magnitudes and spectra increases our ability to constrain the object temperature. For ULAS 0034 and 1335 the bolometric flux is well constrained and the width of the temperature range obtained (150–200 K) is mainly due to the radius. Using the NIR spectrum and photometry only, the uncertainty on the flux increases and the temperature range obtained doubles.

To have an idea of the eventual systematics, we also tested the technique described in Cushing et al. (2008), e.g. to fit the object spectrum using the model spectra. The best fit spectrum was selected as the one that minimize:

$$G_{\rm k} = \sum_{i=1}^{n} w_i \left(\frac{f_i - C_{\rm k} F_{\rm k,i}}{\sigma_{\rm i}} \right)^2 \qquad (2)$$

where n is the number of data pixels, $f_{\rm i}$ is the measured flux in the i-th spectral interval, $C_{\rm k}$ is the scaling factor $(R/d)^2$, $F_{\rm k,i}$ is

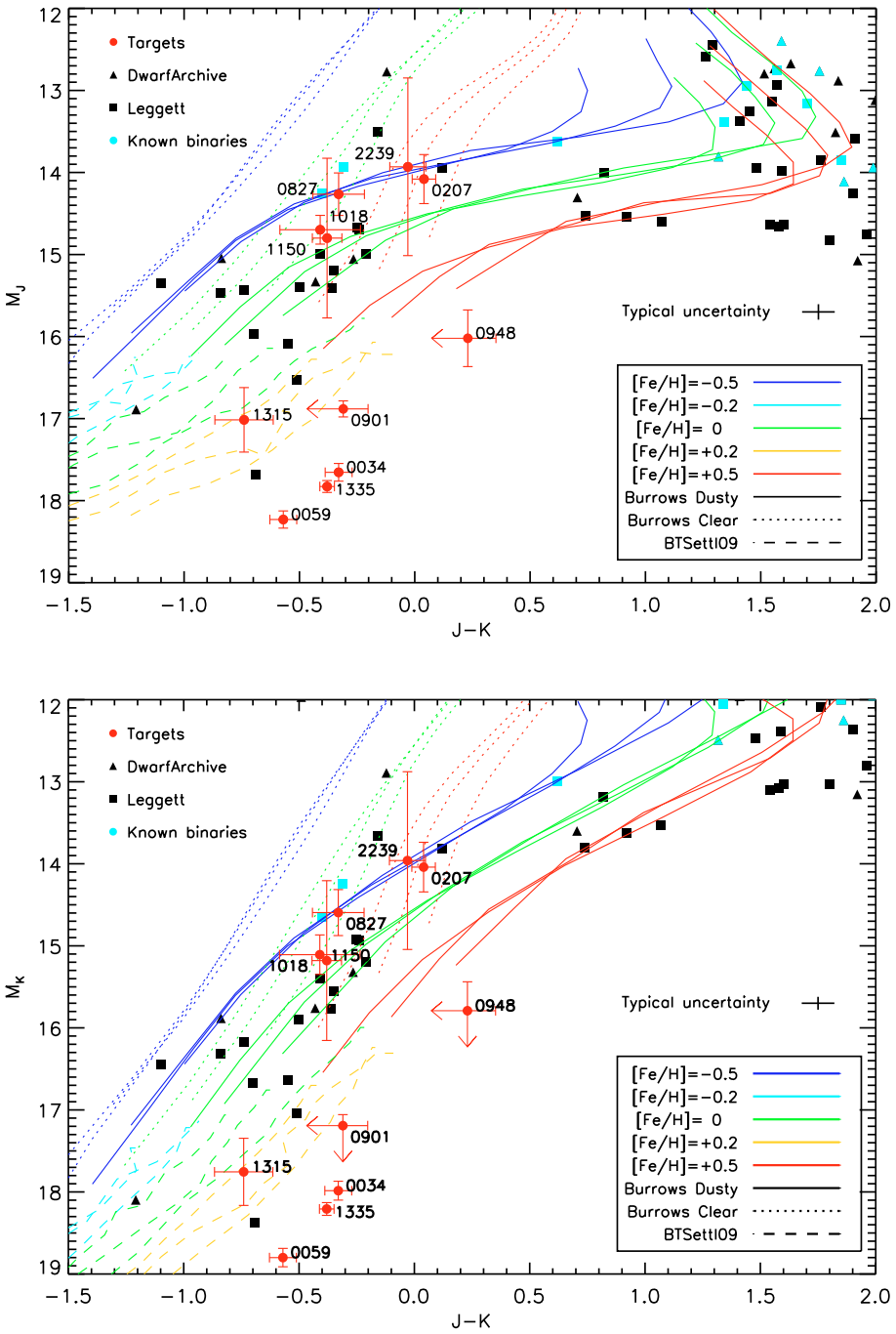

Fig. 3. Same as Fig. 2 but with the color $J - K$ instead of $J - H$. For each metallicity, the gravity increases from right to left, assuming the values 4.5,5.0,5.5 for BSH06 tracks and 4.5,5.0,5.25 for BTSettl09.

the k-th model flux and σ_i is the error in the measured spectrum. The weight associated to each bin (w_i) is the extension of the bin itself ($\Delta\lambda$) as suggested by Cushing et al. The scaling factor can be provided by the fit, however, since we know the distance to the dwarf we consider fixed values of C_k, assuming again the radius range previously indicated. We selected the best fit models for the two extreme configurations, i.e. 0.5 Gyr–1.2 $R_{\rm Jup}$ and 10 Gyr–0.8 $R_{\rm Jup}$.

Since we don't have an associated noise spectrum for ULAS 0827, 0948, 1018, 1150, 1315 and CFBDS 0059 we minimize:

$$G_k = \sum_{i=1}^{n} w_i \left(\frac{f_i - C_k F_{k,i}}{\sqrt{f_i}} \right)^2 \quad (3)$$

The uncertainty in the extremes takes into account half of the models grid spacing based on fitting (for further details see Cushing et al.), plus an additional percentage on the flux due to the incomplete spectral coverage. This percentage was estimated comparing the measured IRAC magnitudes of ULAS 0034 and 1335 with the model's predicted ones. The differences between measured and model magnitudes gives an average uncertainty of ~70% on the calculated flux between 2.5 and 7.5 μm. For ULAS 0034 and 1335 in this interval there is ~40% of the total emergent flux, so we obtain a relative error $\sigma_{\rm F,rel} = .7 \times .4 = .28$. This implies an additional uncertainty of ~7% on the temperature. For the other 9 objects, the uncertainty in the temperature was estimated extending the relative sigma calculated for ULAS 0034 and 1335 to the uncovered part of the flux (~60%, that results in an uncertainty $\sigma_{\rm F}$, rel = $.7 \times .6 = .42$).

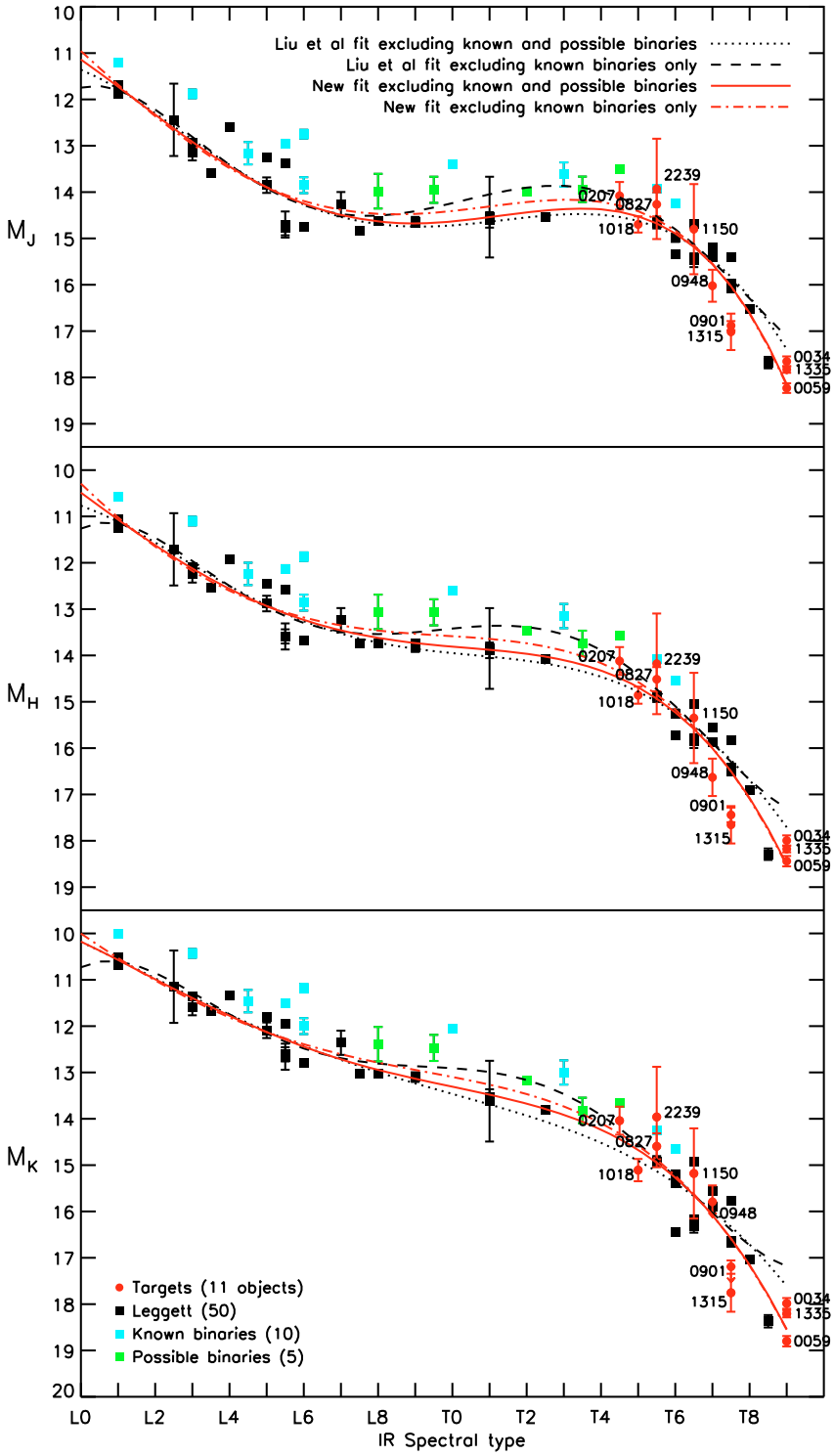

Fig. 4. *J*, *H* and *K*-band absolute magnitude as a function of IR spectral type. Labeled objects are those with new parallaxes presented here. Blue squared points are known to be unresolved binaries, while green squared points are possible unresolved binaries. The over plotted lines are polynomial fit by Liu et al. (2006) based on data tabulated by Knapp et al. (2004). The dotted line was obtained excluding all the known and possible binaries, the dashed one excluding only the known binaries. The red lines are our new polynomial fits.

The choice of the weight function is arbitrary. Different choices can lead to different results, as seen by Cushing et al. (2008) and Stephens et al. (2009). Given this, we prefer the results obtained with the first method described. The values obtained with this spectral technique are summarized in Table 7. They are largely consistent with the ones obtained scaling the model spectra.

We also performed a completely model independent flux calculation for ULAS 0034 and 1335, that have a completely measured spectral energy distribution. We determined the bolometric flux emitted integrating the measured spectrum between 1 and 2.5 μm, then adding the flux emitted between 2.5 and 7.5 μm calculated using the IRAC magnitudes (assuming a constant flux distribution over the passband[2]), finally we integrated the measured 7.5–15 μm spectrum. The flux emitted beyond 15 μm was estimated assuming a Rayleigh-Jeans tail. The results obtained for ULAS 0034 and 1335 with this approach are consistent with

[2] The error introduced by this assumption is of the order of 20% on the flux, so 5% in the temperature, that is within our errors.

Table 4. Coefficients of the polynomial fit.

Magnitude	a_0	a_1	a_2	a_3	a_4
Excluding known and possible binaries					
M_J	11.140 ± 0.052	0.556 ± 0.032	$3.74 \pm 0.62 \times 10^{-2}$	$-9.49 \pm 0.45 \times 10^{-3}$	$3.69 \pm 0.11 \times 10^{-4}$
M_H	10.486 ± 0.051	0.590 ± 0.031	$-3.80 \pm 0.61 \times 10^{-3}$	$-4.35 \pm 0.44 \times 10^{-3}$	$2.15 \pm 0.11 \times 10^{-4}$
M_K	10.180 ± 0.056	0.375 ± 0.035	$2.31 \pm 0.67 \times 10^{-2}$	$-5.03 \pm 0.49 \times 10^{-3}$	$2.11 \pm 0.12 \times 10^{-4}$
Excluding known binaries					
M_J	10.957 ± 0.053	0.736 ± 0.032	$-5.53 \pm 0.61 \times 10^{-3}$	$-6.31 \pm 0.44 \times 10^{-3}$	$2.96 \pm 0.11 \times 10^{-4}$
M_H	10.292 ± 0.052	0.778 ± 0.031	$-4.77 \pm 0.60 \times 10^{-2}$	$-1.13 \pm 0.43 \times 10^{-3}$	$1.41 \pm 0.10 \times 10^{-4}$
M_K	10.005 ± 0.056	0.548 ± 0.034	$-1.84 \pm 0.64 \times 10^{-2}$	$-1.93 \pm 0.46 \times 10^{-3}$	$1.38 \pm 0.11 \times 10^{-4}$

Notes. The fits are defined as in Liu et al. (2006): $M_{XX} = \sum_{i=0}^{4} a_i \times (\mathrm{SpT})^i$ where XX indicates J, H or K-band magnitude and the spectral types are defined following the convention SpT = 1 for L1, SpT = 9 for L9, SpT = 10 for T0 etc. The fit is valid for spectral types from L0 to T9. Infrared spectral types are used for both L and T dwarfs.

the one obtained with the other techniques described within the uncertainty quoted in Table 6.

6. Discussion

In Fig. 6 we present a $T_{\rm eff}$-spectral type diagram of the 11 T-dwarfs of the sample, for each of which we plot the temperature range displayed in Table 6. When needed, objects have been offset by ±0.1 in spectral type, to avoid overlaps. Over plotted for comparison we have the effective temperature – infrared type relation derived by Stephens et al. (2009). All the ranges are consistent with the relation except for ULAS 0948, 0901 and 1315, that are cooler than predicted.

We now discuss individual objects with temperature values or indications of peculiarity in the literature.

6.1. ULAS 0034

There are several estimations of the temperature of this object. In the discovery paper, Warren et al. (2007) estimate a conservative range of $600 \leq T_{\rm eff} \leq 700$ K using the measured NIR spectrum and the near- and mid-infrared photometry with a grid of solar-abundance BTSettl model, calibrated using the parameters of 2MASS0415, and a linear fit of $T_{\rm eff}$ vs. H-[4.5] color for hotter stars; Delorme et al. (2008) using the NIR spectrum and the same grid described in Warren et al. (2007) determine $T_{\rm eff} \approx 670$ K; in Leggett et al. (2009) the published range is $550 \leq T_{\rm eff} \leq 600$, obtained fitting the measured NIR and MIR spectrum with model spectra by Saumon & Marley (2008); finally, in SJL10 using the parallax reported in this paper and the model fitting in Leggett et al. (2009), using a model radius of 0.11 $R_\odot$ (as implied by the spectral fits constraints on gravity), derive a bolometric luminosity of $L/L_\odot = 1.10 \pm 0.01 \times 10^{-6}$, consistent with the temperature range 550–600 K. In this work, using NIR and MIR spectrum, the MKO NIR photometry and the IRAC MIR photometry, we find a luminosity of $L/L_\odot = 1.13 \pm 0.06 \times 10^{-6}$, consistent with the value obtained by Leggett et al. (2009). The difference between the temperature range derived here and by Leggett et al. is due to the different technique used: the Leggett et al. spectral fitting result is similar to that derived spectrally here, given in Table 7.

6.2. CFBDS 0059

In the discovery paper (Delorme et al. 2008) of this object they estimate $T_{\rm eff} \sim 620$ K comparing the spectral indices with a solar metallicity grid of BTSettl model spectra. In Leggett et al. (2009) the technique adopted is the same described in Sect. 6.1, and the range obtained is $550 < T_{\rm eff} < 600$. Here we found a range $490 < T_{\rm eff} < 600$ consistent with Leggett et al., larger because of the different technique used. Moreover, as noted in Delorme et al. (2008) using the Besançon stellar population model (Robin et al. 2003), the kinematics suggest that the target is a older member of the thin disk (age ∼ 4 Gyr) that corresponds, using Baraffe et al. (2003) radii, to a radius $R \approx 0.9\ R_{\rm Jup}$ and a $T_{\rm eff} \approx 570$ K. As regards its gravity and metallicity, we noted in Sect. 4 that the model predictions are not consistent, so we do not go further in the analysis of these physical properties.

6.3. SDSS 0207

In Vrba et al. (2004) they find a $\pi_{\rm abs} = 34.85 \pm 9.87$ mas and $\mu_{\rm tot} = 156.3 \pm 11.4$ mas/yr for SDSS 0207, both consistent with the values found here. The model predictions in Figs. 2 and 3 indicates $\log[g] = 5.0$ and low or solar metallicity while the BSH06 clear tracks indicates a metal-rich nature in $J - K$.

There are two previous estimates of effective temperature for this object: Golimowski et al. (2004), using the measured spectrum and estimating the bolometric correction using M' and L' photometry, find $L_{\rm bol}/L_\odot = 1.51 \pm 0.87 \times 10^{-5}$; Vrba et al. (2004) using the K-band magnitude and the bolometric correction derived by Golimowski et al. and find $L_{\rm bol}/L_\odot = 1.74 \pm 1.04 \times 10^{-5}$. Both these values are consistent with our result.

6.4. ULAS 0901

ULAS 0901 is much cooler than what expected for its type, see Fig. 6. In Fig. 4 the dwarf is fainter than the other T7.5 s of the sample, in particular in M_J and $M_{\rm H}$. This maybe an indication that ULAS 0901 is half a subclass later, i.e. a T8.

In Lodieu et al. (2007) ULAS 0901 is indicated as a high gravity – solar metallicity object, based on the low K-band flux. The model prediction of the gravity and the metallicity of this object in Figs. 2 and 3 are $\log[g] = 4.5$ and [Fe/H] = + 0.2 (in contrast with this finding) but we must point out the known degeneracy between gravity and metallicity (Knapp et al. 2004). This degeneracy could be the reason for the discrepancy between our result and Lodieu et al.

6.5. ULAS 1018

The model predictions in Figs. 2 and 3 are not consistent for ULAS 1018. In the $J - K$ space it appears as a solar-metallicity low-gravity ($\log[g] = 4.5$) object, while the $J - H$ prediction

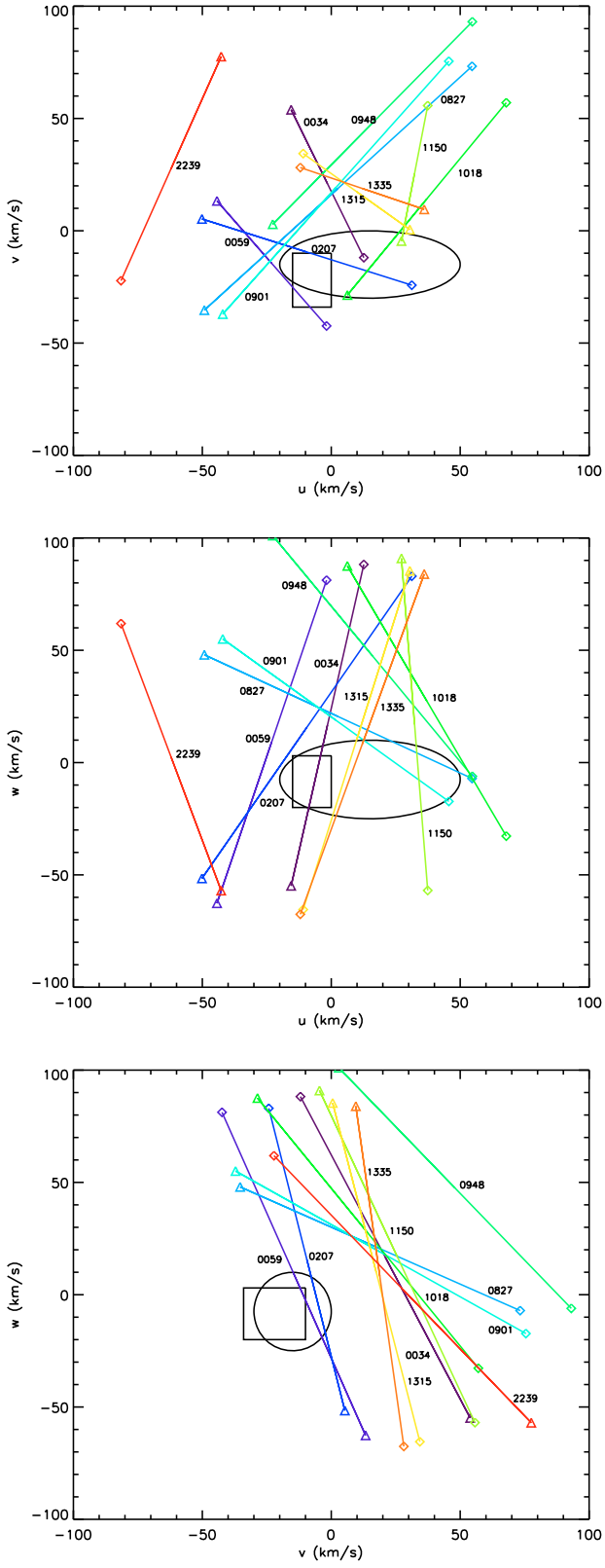

Fig. 5. The galactic velocity components U, V and W obtained from the proper motions in Table 2 assuming a V_{rad} range of +80/–80 km s^{-1}. The triangle indicates the +80 km s^{-1} extreme, the diamond indicates the –80 km s^{-1} extreme. The overplotted black box is the locus of young stars (Zuckerman & Song 2004, age < 0.1 Gyr), the ellipsoid is the locus of young disk stars (Eggen 1969, age < 0.5 Gyr).

Table 5. IRAC magnitudes of ULAS 0034, SDSS 0207 and ULAS 1335 (Warren et al. 2007; Patten et al. 2006; Burningham et al. 2008) used to scale the model spectra.

	ULAS 0034	SDSS 0207	ULAS 1335
3.55 μm	16.28 ± 0.49	15.59 ± 0.06	15.96 ± 0.48
4.49 μm	14.49 ± 0.43	14.98 ± 0.05	13.91 ± 0.42
5.73 μm	14.82 ± 0.44	14.67 ± 0.20	14.34 ± 0.43
7.87 μm	13.91 ± 0.42	14.17 ± 0.19	13.37 ± 0.41

is low-gravity and low-metallicity ([Fe/H] = – 0.5). The uncertainty in color and magnitude prevent us to draw a firm conclusion on the properties of this object. We mention here that ULAS 1018 is indicated as a metal-poor object by Murray et al. (in prep.) based on its very blue $H - K$, while in Lodieu et al. (2007), was indicated as a possible metal-rich object, based on the high K-band flux and narrow Y-band flux peak.

The bolometric luminosity and thus the temperature range obtained are consistent with an object of spectral type T5.

6.6. ULAS 1150

This object is a peculiar T6.5, with T7-T6.5 indices in the J and K band (H_2O–J = 0.087, $CH_4 - J$ = 0.302, CH_4–K = 0.032, Pinfield et al. 2008), but T3 in the H (H_2O–H = 0.455). Pinfield et al. suggest that it could be a low-gravity high-metallicity object, based on the K-band enhancement and the Y-band suppression. In Fig. 2 it assumes an anomalous position, lying on the low-gravity high-metallicity side of the theoretical curves while in Fig. 3 the model predicts a low/solar metallicity. The large errors prevent us from making any comments on its gravity.

The bolometric luminosity and thus the temperature range obtained are consistent with an object of spectral type T6.5.

6.7. ULAS 1315

In Fig. 6 it appears significantly cooler than the other T7.5s. In the discovery paper, Pinfield et al. (2008), no particular indication of peculiarity were detected. Looking at Figs. 2 and 3 it is easy to see that ULAS 1315 is particularly faint in M_K (it is the bluest in $J-K$), and the K-band suppression indicates high gravity, as predicted by the models. However the indication of high metallicity in the same plots is in contradiction with this interpretation as a metal-rich object would show an enhancement in the K-band flux. It is fainter than the other T7.5 s also in M_J and M_H, this results in an extremely cool temperature, almost 200 K less than what expected. This can indicate that ULAS 1315 is a T8 (the spectral indices H_2O-J, CH_4-J and CH_4-H corresponds to a T8, while H_2O-H to a T7, see Pinfield et al. 2008).

6.8. ULAS 1335

There are two previous estimations of the temperature of this object: Burningham et al. (2008), using a solar-metallicity BTSettl model grid and a comparison of the H–[4.49] color with theoretical expectations, find $T_{\rm eff} \sim$ 550–600 K; Leggett et al. (2009), using the technique described in Sec. 6.1, find $T_{\rm eff}$ = 500–550 K. The luminosity obtained here ($L_{\rm bol} = 1.09 \pm 0.06 \times 10^{-6}\ L_\odot$) is formally consistent with both those ranges, given the large uncertainty in the radius, but it is closer to the value obtained in Burningham et al. (2008). As in the case of the other late T dwarfs, ULAS 0034 and CFBDS 0059, the model predictions are contradictory in the different color spaces and we are

Table 6. Fluxes, luminosities and temperatures of the sample obtained scaling the model spectra using the measured magnitudes, e.g. the first method discussed in Sect. 5.

Object	Sp. Type	Est. $T_{\rm eff}$ (K)	Models used (K)	1st step (K)	2nd step (K)	$F_{\rm bol}$ (erg s^{-1} cm^{-2})	$L/L_{\odot}$	$T_{\rm eff}$ range (σ) (K)
ULAS 0034	T9	500	500:700	540:700	540:660	$2.34 \pm 0.05 \times 10^{-13}$	$1.13 \pm 0.06 \times 10^{-6}$	535–660 (35)
CFBDS 0059	T9	500	500:700	500:620	500:620	$2.85 \pm 0.48 \times 10^{-13}$	$7.20 \pm 1.25 \times 10^{-7}$	480–590 (55)
SDSS 0207	T4.5	1130	900:1400	1000:1400	1100:1200	$4.98 \pm 0.26 \times 10^{-13}$	$1.72 \pm 0.25 \times 10^{-5}$	1060–1300 (110)
ULAS 0827	T5.5	1070	900:1300	1000:1300	1000:1100	$2.87 \pm 0.09 \times 10^{-13}$	$1.21 \pm 0.15 \times 10^{-5}$	970–1190 (95)
ULAS 0901	T7.5	830	600:1000	600:700	600:700	$1.88 \pm 0.15 \times 10^{-14}$	$1.42 \pm 0.13 \times 10^{-6}$	570–700 (50)
ULAS 0948	T7	910	700:1100	700:800	700:800	$6.52 \pm 0.44 \times 10^{-14}$	$2.61 \pm 0.44 \times 10^{-6}$	660–810 (80)
ULAS 1018	T5	1100	900:1300	900:1100	900:1000	$1.80 \pm 0.43 \times 10^{-13}$	$8.54 \pm 0.70 \times 10^{-6}$	890–1090 (75)
ULAS 1150	T6.5p	980	800:1200	800:1200	900:1000	$6.76 \pm 0.40 \times 10^{-14}$	$7.12 \pm 3.22 \times 10^{-6}$	850–1040 (160)
ULAS 1315	T7.5	830	600:1000	600:740	600:660	$7.47 \pm 0.72 \times 10^{-14}$	$1.21 \pm 0.25 \times 10^{-6}$	545–670 (70)
ULAS 1335	T9	500	500:700	540:660	540:660	$3.42 \pm 0.09 \times 10^{-13}$	$1.09 \pm 0.06 \times 10^{-6}$	530–650 (35)
ULAS 2239	T5.5	1070	900:1300	900:1300	1100:1200	$6.00 \pm 0.09 \times 10^{-14}$	$1.65 \pm 0.82 \times 10^{-5}$	1050–1280 (200)

Table 7. Temperatures obtained fitting the observed spectrum, e.g. the second method discussed in Sect. 5.

Name	Sp. Type	$T_{\rm eff}$ range (σ) (K)
ULAS 0034	T9	500–580 (40)
CFBDS 0059	T9	500–540 (60)
SDSS 0207	T4.5	1000–1200 (120)
ULAS 0827	T5.5	1100–1200 (130)
ULAS 0901	T7.5	620–720 (75)
ULAS 0948	T7	700–800 (90)
ULAS 1018	T5	900–1100 (120)
ULAS 1150	T6.5p	800–1000 (110)
ULAS 1315	T7.5	540–620 (65)
ULAS 1335	T9	500–600 (40)
ULAS 2239	T5.5	1100–1300 (135)

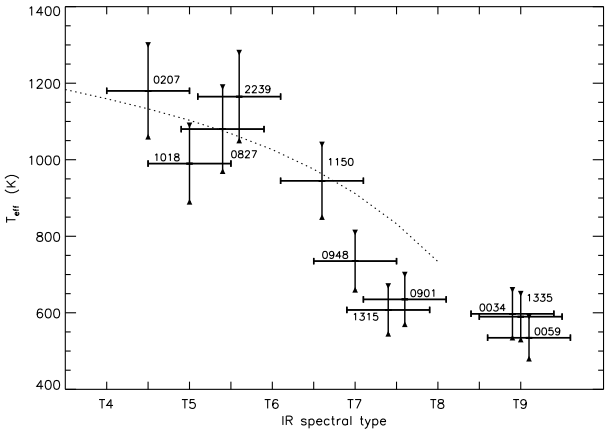

Fig. 6. Temperature ranges plotted as a function of the spectral type. Uncertainties in each extreme point of the range are in Table 6. The uncertainty in spectral type is half subtype. The over plotted dotted line is the effective temperature-infrared type relation derived by Stephens et al. (2009).

therefore unable to say anything about the other parameters of this objects.

7. Conclusions

We present the parallax and proper motions of 11 cool T dwarfs taking advantage of the UKIDSS discovery image to shorten the time required for a precise determination. We find that the models do not predict the colors and absolute magnitudes of the coolest T dwarfs, and that, given the observed colors and absolute magnitudes, the models predict contradictory behaviours depending on which color is considered.

We examine two methods for the calculation of $T_{\rm eff}$, one of which derives the temperature from the luminosity, which is determined using available spectroscopic data complemented with model spectra scaled using measured photometry, and the other of which does a least-squares-like model spectrum fit to the observed spectrum. The second method is very dependent on the data weighting selection and so we prefer the former technique. The two approaches give consistent results however the former gives a larger range in temperature.

The observations of these 11 objects are continuing at a lower frequency of 4 observations per year. At the end of the observing campaign all the objects in the sample will have a time coverage of 4 years, allowing us to obtain a more precise and robust parallax solution. Also, enhanced photometry for ULAS 0901 and ULAS 0948 is expected within the year.

The inclusion of MIR observations increases our ability to determine the object parameters, especially for the temperature. With IRAC photometry and a MIR spectrum the emitted flux is well constrained and the limiting factor becomes the radius, producing a range of ~150 K. Using a NIR spectrum and photometry only, the uncertainty in the flux is on the order of that on the radius, and the temperature range obtained doubles. For the future we hope that the Warm-Spitzer and WISE missions will continue to provide MIR observations for the study of these objects.

Acknowledgements. The authors would like to acknowledge the support of: the Royal Society International Joint Project 2007/R3; the PARSEC International Incoming Fellowship and IPERCOOL International Research Staff Exchange Scheme within the Marie Curie 7th European Community Framework Programme. This research has benefitted from the M, L, and T dwarf compendium housed at dwarfArchives.org and maintained by Chris Gelino, Davy Kirkpatrick, and Adam Burgasser. The United Kingdom Infrared Telescope is operated by the Joint Astronomy Centre on behalf of the Science and Technology Facilities Council of the UK, all of the data used here were obtained as part of the UKIRT Service Programme. S.K.L.'s research is supported by the Gemini Observatory, which is operated by the Association of Universities for Research in Astronomy, Inc., on behalf of the international Gemini partnership of Argentina, Australia, Brazil, Canada, Chile, the United Kingdom, and the United States of America. N.L. acknowledges funding from the Spanish Ministry of Science and Innovation through the Ramón y Cajal fellowship number 08-303-01-02.

References

Allard, N. F., Allard, F., Hauschildt, P. H., Kielkopf, J. F., & Machin, L. 2003, A&A, 411, L473
Allard, F., Allard, N. F., Homeier, D., et al. 2007, A&A, 474, L21
Allard, N. F., Noselidze, I., & Kruk, J. W. 2009, A&A, 506, 993
Baraffe, I., Chabrier, G., Barman, T. S., Allard, F., & Hauschildt, P. H. 2003, A&A, 402, 701
Burgasser, A. J., Geballe, T. R., Leggett, S. K., Kirkpatrick, J. D., & Golimowski, D. A. 2006a, ApJ, 637, 1067
Burgasser, A. J., Kirkpatrick, J. D., Cruz, K. L., et al. 2006b, ApJS, 166, 585
Burgasser, A. J., Tinney, C. G., Cushing, M. C., et al. 2008, ApJ, 689, L53
Burningham, B., Pinfield, D. J., Leggett, S. K., et al. 2008, MNRAS, 391, 320
Burningham, B., Pinfield, D. J., Lucas, P. W., et al. 2010, MNRAS, 821
Burrows, A., Marley, M., Hubbard, W. B., et al. 1997, ApJ, 491, 856
Burrows, A., Sudarsky, D., & Hubeny, I. 2006, ApJ, 640, 1063
Chiu, K., Liu, M. C., Jiang, L., et al. 2008, MNRAS, 385, L53
Cushing, M. C., Marley, M. S., Saumon, D., et al. 2008, ApJ, 678, 1372
Delorme, P., Delfosse, X., Albert, L., et al. 2008, A&A, 482, 961
Eggen, O. J. 1969, PASP, 81, 553
Geballe, T. R., Knapp, G. R., Leggett, S. K., et al. 2002, ApJ, 564, 466
Golimowski, D. A., Leggett, S. K., Marley, M. S., et al. 2004, AJ, 127, 3516
Harrington, R. S., & Dahn, C. C. 1980, AJ, 85, 454
Hewett, P. C., Warren, S. J., Leggett, S. K., & Hodgkin, S. T. 2006, MNRAS, 367, 454
Hubeny, I., & Burrows, A. 2007, ApJ, 669, 1248
Kendall, T. R., Tamura, M., Tinney, C. G., et al. 2007, A&A, 466, 1059
Knapp, G. R., Leggett, S. K., Fan, X., et al. 2004, AJ, 127, 3553
Lawrence, A., Warren, S. J., Almaini, O., et al. 2007, MNRAS, 379, 1599
Leggett, S. K., Cushing, M. C., Saumon, D., et al. 2009, ApJ, 695, 1517
Leggett, S. K., Burningham, B., Saumon, D., et al. 2010, ApJ, 710, 1627
Liu, M. C., Leggett, S. K., Golimowski, D. A., et al. 2006, ApJ, 647, 1393
Lodieu, N., Pinfield, D. J., Leggett, S. K., et al. 2007, MNRAS, 379, 1423
Lodieu, N., Burningham, B., Hambly, N. C., & Pinfield, D. J. 2009a, MNRAS, 397, 258
Lodieu, N., Dobbie, P. D., Deacon, N. R., Venemans, B. P., & Durant, M. 2009b, MNRAS, 395, 1631
Nakajima, T., Oppenheimer, B. R., Kulkarni, S. R., et al. 1995, Nature, 378, 463
Patten, B. M., Stauffer, J. R., Burrows, A., et al. 2006, ApJ, 651, 502
Perryman, M. A. C., Lindegren, L., Kovalevsky, J., et al. 1997, A&A, 323, L49
Pinfield, D. J., Burningham, B., Tamura, M., et al. 2008, MNRAS, 390, 304
Robin, A. C., Reylé, C., Derrière, S., & Picaud, S. 2003, A&A, 409, 523
Saumon, D., & Marley, M. S. 2008, ApJ, 689, 1327
Saumon, D., Marley, M. S., Cushing, M. C., et al. 2006, ApJ, 647, 552
Smart, R. L., Jones, H. R. A., Lattanzi, M. G., et al. 2010, A&A, 511, A30
Stephens, D. C., & Leggett, S. K. 2004, PASP, 116, 9
Stephens, D. C., Leggett, S. K., Cushing, M. C., et al. 2009, ApJ, 702, 154
Tokunaga, A. T., Simons, D. A., & Vacca, W. D. 2002, PASP, 114, 180
Vrba, F. J., Henden, A. A., Luginbuhl, C. B., et al. 2004, AJ, 127, 2948
Warren, S. J., Mortlock, D. J., Leggett, S. K., et al. 2007, MNRAS, 381, 1400
Zuckerman, B., & Song, I. 2004, ARA&A, 42, 685